Renewable Energy 160 (2020) 127–135

Contents lists available at ScienceDirect

Renewable Energy

journal homepage: www.elsevier.com/locate/renene

Regional measurements to analyze large-area luminescent solar concentrators

Yilin Li [a, *], Yujian Sun [b], Yongcao Zhang [c]

[a] Department of Chemical and Biomolecular Engineering, Rice University, Houston, TX, 77005, United States
[b] School of Environmental and Forest Sciences, University of Washington, Seattle, WA, 98195, United States
[c] Department of Mechanical Engineering, University of Houston, Houston, TX, 77004, United States

ARTICLE INFO

Article history:
Received 9 April 2020
Received in revised form
16 June 2020
Accepted 24 June 2020
Available online 28 June 2020

Keywords:
Luminescent solar concentrator
Large-area
Photovoltaic performance
Photon transport mechanism
Common laboratory instruments
Monte Carlo ray-tracing simulation

ABSTRACT

Experimentally analyzing the photovoltaic (PV) performance and the photon transport mechanism of large-area luminescent solar concentrators (LSCs) (>200 cm^2) has proven difficult because common solar simulators and integrating spheres have limited measuring capacity. This report introduces an approach of regional measurements to address these issues using common laboratory instruments. In this approach, the LSC is configured to have different surface and edge regions. The surface regions are sequentially illuminated by a low-cost solar simulator, and the edge regions sequentially measured by a small-area solar cell or a general photoluminescence (PL) spectrometer. The methodology is validated through the comparison with the conventional method and Monte Carlo ray-tracing simulation in the study of the PV performance of a series of R305-based LSCs. Experimental results from the regional measurements reveal important the photon transport mechanism of the LSCs. The results show that severe photon transport loss exists within a surface distance (d_{surf}) of 5 inches (12.7 cm), and photons with the longest average transport distance ($<L_{ptn}>_{max}$) experience number of absorption events (N_{abs}) for an average of 11.3 times. The approach of regional measurements can effectively measure the PV performance and investigate the photon transport mechanism of large-area LSCs.

1. Introduction

Luminescent solar concentrators (LSCs) have attracted a lot of attention in the past decades because they are promising for seamlessly integrating photovoltaic (PV) technologies into the built environment [1–5]. A typical LSC consists of a planar optical waveguide doped with luminophores and becomes a PV device when configured with edge-attached solar cells as shown in Fig. 1. During the operation, sunlight is absorbed by the luminophores and converted to luminescent light, which transports to the solar cell through successive total internal reflection (TIR). This design significantly reduces the material use of solar cells and enables a variety selection of device appearance [6–8], and therefore makes the LSCs promising for building-integrated photovoltaics (BIPVs) such as power windows [9–11] to generate onsite renewable energy [12–17]. Besides, the capability to work under different light conditions allows the LSCs to access places where conventional solar cells cannot [18], especially some outdoor places with large shaded areas [19] and some indoor places with weak illumination areas [20].

One of the major tasks in the current research of LSC is to enhance the device PV performance, especially the power conversion efficiency (PCE). To this end, researchers have developed various types of luminophores and techniques. Organic dyes [21–23], quantum dots [24–26], rare-earth complexes [27–29], and perovskite nanocrystals [30–32] are four major types of commonly used luminophores. Optical microlens [33–35], plasmonic structures [36–38], wavelength-selective mirrors [39–41], and distributed Bragg reflectors [42–44] are four major categories of photon trapping techniques. Compared with the development of luminophores and techniques for the LSCs, experimental approaches to analyzing LSCs, especially large-area LSCs (>200 cm^2), are very limited. Small-area LSCs (<200 cm^2) are typically characterized using common solar simulators [45–47] and integrating spheres [48–50] in terms of their PV performance and photon transport mechanism. Indeed, most high-efficiency LSCs are devices with very small size (<50 cm^2) and measured using solar simulators that provide small illumination areas (<200 cm^2). Slooff

* Corresponding author.
E-mail address: yilinli@rice.edu (Y. Li).

https://doi.org/10.1016/j.renene.2020.06.121
0960-1481/

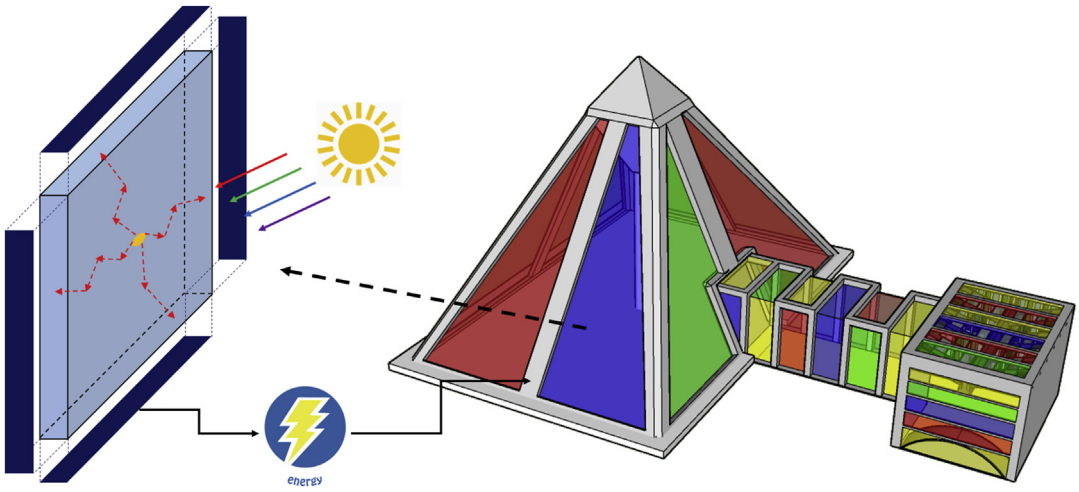

Fig. 1. Schematic images showing the concept, operational mechanism, and application of LSCs.

et al. reported a 25-cm^2 LSC with a PCE of 7.1% achieved through the energy transfer between two luminophores and the use of high-efficiency (>20%) gallium arsenide (GaAs) solar cells [45]. Similarly, Goldschmidt et al. used a tandem device architecture that utilizes different portions of light through different luminophores and obtained a 4-cm^2 LSC with a PCE of 6.7% [46]. Desmet et al. improved the PCE of a 25-cm^2 LSC with monocrystalline silicon solar cells from 3.4% to 4.2% using a microcellular polyethylene terephthalate (MCPET) back reflector [47]. Due to the size limitation of integrating spheres (<15 cm in diameter), the study of the photon transport mechanism is also limited to small-area LSCs. Tummeltshammer et al. analyzed the photon transport loss of a series of 36-cm^2 LSCs using different configurations or their combinations [48]. Furthermore, Klimov et al. performed experimental studies on 4-cm^2 LSCs to validate a theoretical model, which includes a quality factor and calculates practical concentration limits [49]. Frias et al. studied the optical quantum efficiency of a 1-cm^2 LSC based on organic-inorganic hybrids modified with chlorophyll [50]. Different from these studies on small-area LSCs, in which common laboratory instruments are used, large-area LSCs (>200 cm^2) are typically tested in an outdoor environment. For example, Debije and co-workers investigated large-area LSCs as noise barriers in terms of PV, visual, and thermal performance under sunlight in a series of reports [51–53]. These studies on large-area LSCs have shown significant impacts on the practical application of the LSCs. However, they cannot provide information on the photon transport mechanism as common laboratory instruments have limited capacity in characterizing large-area LSCs. The study of large-area LSCs generally requires customized and high-cost large-area solar simulators and large-size integrating spheres, which are not readily available in common laboratories. Some theoretical efforts have also been paid to understand the photon transport mechanism of the LSCs [54–59]. Batchelder et al. modeled the LSCs and found that the luminophore self-absorption is a dominant effect, especially for high-concentration, large-area LSCs [54,55]. Barnham et al. proposed a thermodynamic model to describe the spectroscopic redshift due to the luminophore self-absorption in quantum dot-based LSCs [56]. Wang et al. reported a theoretical study on cylindrical LSCs, which shows higher performance than the conventional square planar LSCs [57]. Joudrier et al. theoretically investigated the LSCs with photonic band stops and validated the results through experiments [58]. Sychugov provided explicit expressions for the LSCs and revealed the loss mechanisms in the LSCs [59]. Though useful insights into the photon transport mechanism are provided by these studies, some key parameters that are derived from these theoretical studies cannot be directly verified through experiments due to the limitation of instrumentations. Therefore, there is a need to develop new methodologies to study large-area LSCs and the photon transport mechanism.

In this report, we propose an approach of regional measurements to analyze large-area LSCs (>200 cm^2) using common laboratory instruments. The experimental details (section 2) include materials and instruments (section 2.1) and the fabrication of the LSCs (section 2.2). In the methodology (section 3), we show the description of the methodology (section 3.1), which contains experimental setup (section 3.1.1), quantification and simplification (section 3.1.2), and surface and edge effects (section 3.1.3). Then we show the validation of the methodology (section 3.2) through the comparison between the conventional method (section 3.2.1) and regional measurements (section 3.2.2) in the measurements of the device PCEs (section 3.2.3). The difference in PCEs is explained through the edge distribution of the short-circuit current (section 3.2.4). In the results and discussion (section 4), we study the PCEs of large-area LSCs (section 4.1), especially the PCEs from the experiment and simulation (section 4.1.1) and the difference in PCEs between the experiment and simulation (section 4.1.2). We also reveal the photon transport mechanism (section 4.2), which includes the relationship between the edge emission wavelength and surface distance (section 4.2.1), and the relationship between the photon transport distance and the number of absorption events (section 4.2.2). This new approach allows investigating the PV performance and photon transport mechanism of large-area LSCs using a low-cost solar simulator, a small-area solar cell, and a general photoluminescence (PL) spectrometer.

2. Experimental details

2.1. Materials and instruments

All chemicals were used as received without further purification. The renowned BASF Lumogen F Red 305 (R305) was chosen as luminophores in the LSCs [60–62], and it was purchased from TCI America. The monomer methyl methacrylate (MMA) and the radical initiator azobisisobutyronitrile (AIBN) were purchased from Sigma-Aldrich. The polycrystalline-silicon (p-Si) solar cells were purchased from eBay. The index-matching fluid was purchased from Newport. The specifications of the materials used in this study

Table 1
The specifications of the materials used in this study.

Material (Source)	Specification
R305 (TCI America)	Purity: > 95.0%
MMA (Sigma-Aldrich)	Purity: 99%. Contains ≤30 ppm MEHQ as an inhibitor
AIBN (Sigma-Aldrich)	Purity: 98%
p-Si solar cells (eBay)	Efficiency: 15.5%
Index-matching fluid (Newport)	Refractive index: 1.52@589nm. Viscosity: 100 cps.

are given in Table 1.

The spectroscopic properties of R305 in poly (methyl methacrylate) (PMMA) and the photovoltaic properties of the solar cells were reported in the literature [20]. The absorption wavelength ($\lambda_{abs,R305}$) and emission wavelength ($\lambda_{em,R305}$) of R305 were 574 nm and 605 nm, respectively. The short-circuit current density ($J_{sc,cell}$), open-circuit voltage ($V_{oc,cell}$), fill factor (FF_{cell}) and power conversion efficiency (PCE) of the solar cell were 330 A m^{-2}, 0.62 V, 0.76 and 15.5%, respectively.

An OAI class AAA solar simulator was used to provide simulated AM1.5G sunlight (1000 W m^{-2}) with 200-cm^2 illumination. In the approach of regional measurements, a low-cost solar simulator with 10-cm^2 illumination was used. Photoluminescence (PL) spectra were recorded on an ISS PC1 photon-counting spectrofluorometer. Monte Carlo ray-tracing simulation was performed according to the models in literature [63–65].

2.2. Fabrication of the LSCs

The LSCs were fabricated according to the literature [23]. The detailed procedures are shown in Fig. 2. A solution of 60 ppm R305 and 0.1 w/w% AIBN in MMA was pre-polymerized at 85 °C for approximately 10 min. The glycerol-like viscous syrup was poured into a glass mold, which had a void space of 14 × 14 × 0.25 in^3 (35.56 × 35.56 × 0.635 cm^3). The mixture in the mold was placed in a convection oven at 45 °C for 48 h for partial polymerization and at 100 °C for 2 h for full polymerization. The resulting raw LSCs were cut and polished by power tools (miter saw and bench polisher) into squares with sizes from 1 inch (2.54 cm) to 12 inches (30.48 cm) and thickness of 0.25 inch (0.635 cm).

In the conventional method for studying small-area LSCs, solar cells were attached to the LSC edge using optically clear epoxy adhesives. The devices were placed in a convection oven for 2 h for curing the adhesives. Solar cells were connected in parallel to maximize the device performance according to the setup in literature [45]. In the approach of regional measurements, an LSC is configured to have different surface and edge regions. The interface between the LSC edge and the solar cell/photoluminescence (PL) spectrometer was filled with index-matching fluid. Surface and edge regions that were not under measurements were coved with a blackout tape.

3. Methodology

3.1. Description of the methodology

3.1.1. Experimental setup

The experimental setup in the regional measurements contains four components, which are a mask, an LSC, a blackout tape, and a solar cell as shown in Fig. 3a. The dimensions and configurations of each component are given in Fig. 3b and described as follows:

(1) Mask. The mask is a square-shaped black sheet with a size from 1 inch (2.54 cm) to 12 inches (30.48 cm). The hole in the mask is a 1-inch (6.4516-cm^2) square. Changing the position of the hole in the mask makes the illumination be on different LSC surface regions.
(2) LSC. The size of the LSC is from 1 inch (2.54 cm) to 12 inches (30.48 cm), and the thickness is 0.25 inch (0.635 cm).
(3) Blackout tape. The length of the blackout tape is from 1 inch (2.54 cm) to 12 inches (30.48 cm), and the width is 0.25 inch (0.635 cm). The blackout tape covers the LSC edge except for the region where the solar cell is attached.
(4) Solar cell. The length of the solar cell is 1 inch (2.54 cm), and the width is 0.25 inch (0.635 cm). Changing the position of the solar cell on the LSC edge allows measuring the photocurrent at different LSC edge regions.

3.1.2. Quantification and simplification

The experiment is quantified and simplified as shown in Fig. 3c. The surface distance (d_{surf}), defined as the distance between the illuminated surface region and the measured edge region, is correlated to the photocurrent (I_{sc}) (Fig. 3c, left image). Geometric symmetry is considered to reduce the experimental effort. For instance, for a 5-inch (161.29-cm^2) LSC, 6 instead of 25 surface regions are illuminated in the experiment (Fig. 3c, right image), and for each illuminated surface region, 25 edge regions were measured. Therefore, 150 sets of data (6 surface regions × 25 edge regions) were collected for a 5-inch (161.29-cm^2) LSC.

3.1.3. Surface and edge effects

The surface and edge effects are also considered in the experiment as shown in Fig. 3d. The surface effect considers the interface between the mask and the LSC surface as shown in Fig. 3e. The edge effect considers the interface between the blackout tape/solar cell and the LSC edge as shown in Fig. 3f. In the experiment, an air gap is

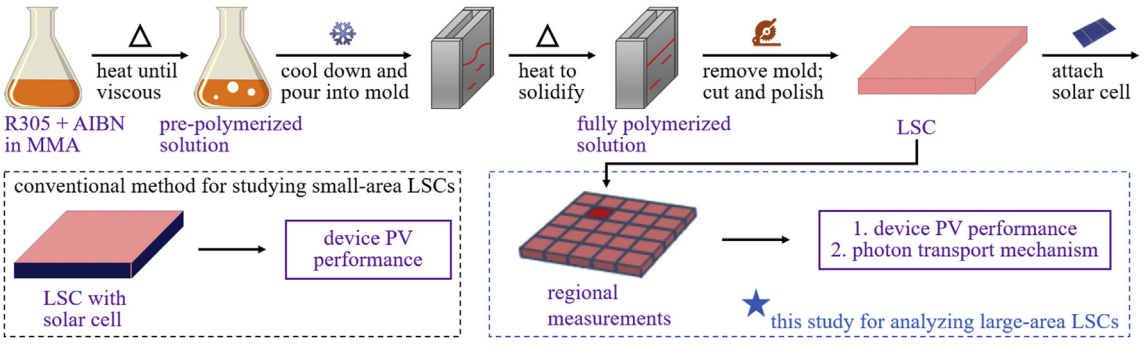

Fig. 2. Schematic images of the fabrication of the LSCs, and the comparison between the conventional method and the approach of regional measurements in this study.

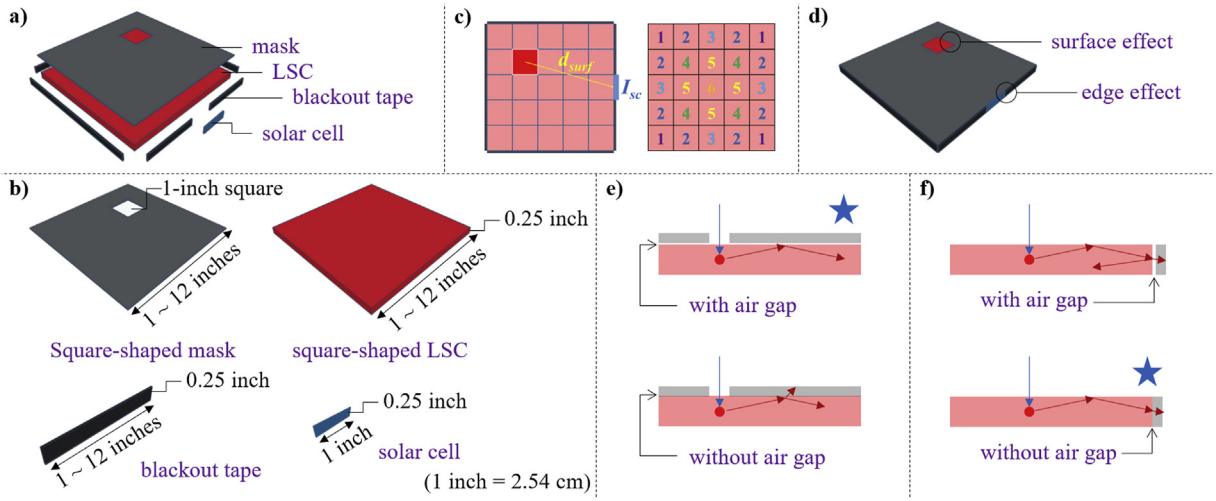

Fig. 3. Schematic images of **a)** experimental setup, **b)** dimensions of each component, **c)** quantification and simplification, **d)** surface and edge effects, **e)** two surface configurations, and **f)** two edge configurations. The stars indicate the configurations used in the experiment.

between the mask and the LSC surface (starred in Fig. 3e) to reduce the photon surface escape, while no air gap is between the blackout tape/solar cell and the LSC edge (starred in Fig. 3f) to improve the photon edge escape. These configurations minimize the photon transport loss during the total internal reflection (TIR) inside the LSC and maximize the photon collection efficiency of the solar cell attached to the LSC edge.

3.2. Validation of the methodology

3.2.1. Conventional method

The approach of regional measurements is validated through the comparison with the conventional method in the study of the PCEs of small-area LSCs (<200 cm^2) with sizes from 1 inch (2.54 cm) to 5 inches (12.7 cm). In the conventional method as shown in Fig. 4a, there is no mask on the LSC surface, and the solar cell covers the whole LSC edge without the air gap. The *J-V* characteristics of the LSCs are shown in Fig. 4b and listed in Table 2. The results indicate that increasing the LSC size does not alter open-circuit voltage (V_{oc}) and fill factor (*FF*) very much. The V_{oc} slightly increases from 0.57 to 0.61, and the FF changes between 0.77 and 0.78. Increasing the LSC size decreases short-circuit current density (J_{sc}) from 52 A m^{-2} to 44 A m^{-2} due to the increase of photon transport loss during TIR inside the LSC, and the corresponding device PCE decreases from 2.27% to 2.04%.

3.2.2. Regional measurements

In the approach of regional measurements where different surface and edge regions are studied in the experimental setup as shown in Fig. 4c, different surface and edge configurations are used, and therefore it is important to consider the surface and edge effects. The configurations of the LSC surface and edge are shown in

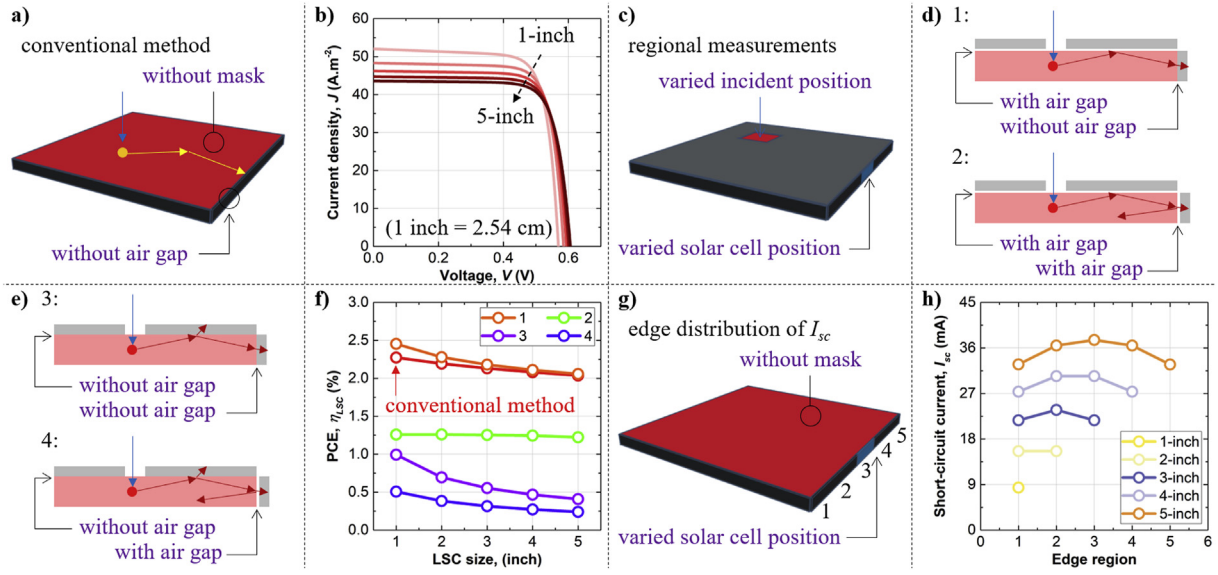

Fig. 4. Experimental setup and results of small-area LSCs (<200 cm^2) with sizes from 1 inch (2.54 cm) to 5 inches (12.7 cm) for the validation of the methodology. **a)** Experimental setup of the conventional method. **b)** *J-V* characteristics of the LSCs. **c)** Experimental setup of the regional measurements. **d)** Surface and edge configuration 1 and 2. **e)** Surface and edge configuration 3 and 4. **f)** PCEs of the LSCs from the regional measurements with different surface and edge configurations compared with those from the conventional method. **g)** Experimental setup to measure the edge distribution of I_{sc}. **h)** Measured edge distribution of I_{sc} of the LSCs.

Table 2
Photovoltaic parameters of the small-area LSCs (<200 cm^2) from the *J-V* characteristics in Fig. 4b.

LSC size (front surface area)	J_{sc} ($A \cdot m^{-2}$)	V_{oc} (V)	*FF*	PCE (%)
1-inch (6.4516-cm^2)	52	0.57	0.77	2.27
2-inch (25.8064-cm^2)	48	0.59	0.78	2.19
3-inch (58.0644-cm^2)	46	0.60	0.78	2.13
4-inch (103.2256-cm^2)	45	0.60	0.77	2.08
5-inch (161.29-cm^2)	44	0.61	0.77	2.04

Fig. 4d and described as follow:

(1) Configuration 1. The air gap exists between the mask and the LSC surface, while it does not exist between the blackout tape/solar cell and the LSC edge. This configuration improves the photon transport inside the LSC and the photon delivery to the LSC edge.
(2) Configuration 2. The air gap exists between the mask and the LSC surface, and it also exists between the blackout tape/solar cell and the LSC edge. This configuration improves the photon transport inside the LSC but disturbing photon delivery to the LSC edge.
(3) Configuration 3. The air gap does not exist between the mask and the LSC surface, and it also does not exist between the blackout tape/solar cell and the LSC edge. This configuration disturbs the photon transport inside the LSC but improving the photon delivery to the LSC edge.
(4) Configuration 4. The air gap does not exist between the mask and the LSC surface, while it exists between the blackout tape/solar cell and the LSC edge. This configuration disturbs the photon transport inside the LSC and the photon delivery to the LSC edge.

3.2.3. Comparison of the PCEs

In the conventional method, the PCE of the LSC (η_{LSC}) is extracted from the *J-V* characteristic. In the approach of regional measurements, because only I_{sc} of the LSC edge region is measured, the PCE of the LSC is calculated using Eq. (1):

$$\eta_{LSC} = \frac{\sum I_{sc} \times V_{oc,cell} \times FF_{cell}}{\sum A_{in} \times H_{in}} \quad (1)$$

where $\sum I_{sc}$ is the sum of the I_{sc} measured for all the LSC edge regions; $V_{oc,cell}$ is the V_{oc} of the solar cell (i.e., 0.62 V); FF_{cell} is the *FF* of the solar cell (i.e., 0.76); A_{in} is the area of the hole in the mask (i.e., 6.4516 cm^2); and H_{in} is the incident power density (i.e., 1000 W m^{-2}).

The PCEs of the LSCs from the regional measurements with different surface and edge configurations are plotted associated with those from the conventional method as shown in Fig. 4f. The results clearly show that configuration 1 (Fig. 4d) delivers the results (orange line in Fig. 4f) very close to those from the conventional method (red line in Fig. 4f), which validate the methodology and suggest that regional measurements can effectively measure the PCEs of the LSCs. The PCEs for very small (≤2-inch) devices from the approach of regional measurements (orange line in Fig. 4f) are higher those from the conventional method (red line in Fig. 4f) could be due to the difference in solar cell configurations and the experimental errors between the two methodologies, which is a minor issue because very small devices are not practical. For configuration 2 (Figs. 4d), 3 (Fig. 4e), and 4 (Fig. 4e), significantly decreased PCEs are obtained (green, violet, and blue lines in Fig. 4f). This is because these configurations lead to photo transport loss inside the LSC and/or insufficient photon delivery to the LSC edge.

3.2.4. Edge distribution of I_{sc}

The slight difference in the PCEs of the LSCs between the approach of regional measurements (orange line in Fig. 4f) and the conventional method (red line in Fig. 4f) is considered primarily attributable to the unevenly distributed photocurrent (I_{sc}) along the LSC edge. To verify this idea, I_{sc} along the LSC edge is measured without the mask on the LSC surface as shown in Fig. 4g. The results show that the degree of the distribution of I_{sc} along the LSC edge increases with the increase of the LSC size as shown in Fig. 4h. The approach of regional measurements on the LSC edge makes it possible to access the edge distribution of I_{sc} compared with the conventional methods.

4. Results and discussion

4.1. PV performance of large-area LSCs

4.1.1. PCEs of large-area LSCs

After the description and validation of the methodology, the next step is to apply the approach of regional measurements to analyze large-area LSCs (>200 cm^2). Here, LSCs with sizes from 6 inches (15.24 cm) to 12 inches (30.48 cm) are investigated. The PCEs of the large-area LSCs cannot be obtained through the conventional method because common solar simulators cannot provide illumination over 200 cm^2. Instead, they are obtained from the Monte Carlo ray-tracing simulation and then compared with those measured from the regional measurements. The Monte Carlo ray-tracing simulation calculates the photon transport path inside the LSC as shown in Fig. 5a. The results show that the PCEs of the large-area LSCs from the experiment (orange line) are consistent with those from the simulation (red line) as shown in Fig. 5b, despite slightly higher values. With the increase of the LSC size, the PCE decreases due to the increase of the photon transport loss. For the largest (12-inch or 929.0304-cm^2) device, the PCE is approximately 1.83%.

4.1.2. Difference in PCEs

The difference in the PCEs between the experiment and the simulation is less than 1%. The slight difference is due to several reasons. One possible reason is that different parameter values are used to calculate the PCE as shown in Fig. 5c. In the experiment, constant $V_{oc,cell}$ and FF_{cell} (dashed line) are used. while in the simulation, variable V_{oc} and *FF* (solid lines) that depend on the LSC size are used. Another possible reason is that the photocurrent (I_{sc}) is unevenly distributed along the LSC edge as shown in Fig. 5d, as previously discussed in the study of the small-area LSCs (<200 cm^2). With the increase of the LSC size, the distribution of I_{sc} along the LSC edge becomes more and more uneven. For instance, the difference between maximum and minimum of I_{sc} for a 12-inch (929.0304-cm^2) LSC is over 15 mA. It is reasonable to consider that for the LSC size beyond 12 inches, significant unevenly distributed I_{sc} along the LSC edge will be observed.

4.2. Photon transport mechanism

4.2.1. Relationship between the edge emission wavelength and surface distance

Since the photocurrent is measured at varying LSC edge regions under the illumination on varying LSC surface regions in the regional measurements, the correlation between the surface distance (d_{surf}) and the photocurrent (I_{sc}) (as defined in Fig. 3c) can be utilized to investigate the photon transport mechanism. The emission spectrum at a certain LSC edge region ($F_{edge}(\lambda)$) can be

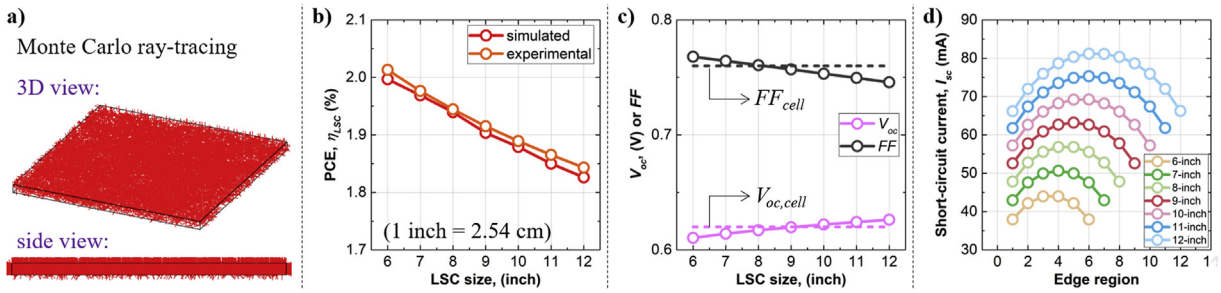

Fig. 5. Studies for the large-area LSCs (>200 cm^2) with size from 6 inches (15.24 cm) to 12 inches (30.48 cm). **a)** Schematic image of the Monte Carlo ray-tracing simulation. **b)** Comparison of the PCEs of the LSCs between the experiment and simulation. **c)** Comparison of the parameters used in the experiment and simulation. **d)** Measured edge distribution of I_{sc} of the LSCs.

calculated using Eq. (2):

$$F_{edge}(\lambda) = \frac{Em(\lambda)}{\int Em(\lambda)d\lambda} \times \frac{I_{sc}}{q \times EQE} \quad (2)$$

where $Em(\lambda)$ is the emission spectrum at the I_{sc}-corresponding LSC edge region measured using a photoluminescence (PL) spectrometer as shown in Fig. 6a; q is the elementary charge (1.6×10^{-19} C); and $<EQE>$ is the average external quantum efficiency of the solar cell between 500 nm and 700 nm (i.e., 0.86) as shown in Fig. 6b.

To demonstrate clear results, 13 representative $F_{edge}(\lambda)$ with d_{surf} from its minimum (0.5 inch or 1.27 cm) to maximum (13.9 inches or 35.306 cm) are shown in Fig. 6c. The results show that along with increased d_{surf}, the intensity of the emission of the edge region decreases while the corresponding emission wavelength (λ_{em}) increases, suggestive of increasing photon transport loss. Since I_{sc} can be converted to $F_{edge}(\lambda)$ and further to obtain λ_{em}, the relationship between d_{surf} and λ_{em} can be established. The result in Fig. 6d shows a clear trend of λ_{em} along with increased d_{surf}, in which λ_{em} increases quickly and then reaches a plateau. The plateau represents the maximum of edge emission wavelength (λ_{em}^{max}), at which the luminophore self-absorption no longer happens. According to the analytical models in the literature [54–59], the relationship between λ_{em} and d_{surf} can be represented using Eq. (3):

$$\lambda_{em} = \lambda_{em}^{max} + \frac{(\lambda_{em,R305} - \lambda_{em}^{max}) \times \sigma}{\sigma + d_{surf}} \quad (3)$$

where λ_{em}^{max} is the maximum of edge emission wavelength as shown in Fig. 6d; $\lambda_{em,R305}$ is the emission wavelength of R305 (i.e., 605 nm) as shown in Fig. 6e; and σ is the luminophore self-absorption cross-section per 1 cm path as shown in Fig. 6e [66].

The dashed line in Fig. 6d represents the fitting results. According to Table 3, the fitting parameter λ_{em}^{max} is 643.9 ± 0.3 nm, which is consistent with that observed from the absorption and emission spectra of R305. Beyond approximate 645 nm, there is almost no spectral overlap and thus no luminophore self-absorption. The other fitting parameter σ is 26.6% ± 4.5%, which well matches the calculated value of 26% from the spectral overlap of R305 [20,67]. The results suggest that the regional measurements can accurately provide parameters that are related to the luminophore self-absorption.

4.2.2. Relationship between the photon transport distance and number of absorption events

To further investigate the photon transport mechanism, Eq. (4) is used to convert $F_{edge}(\lambda)$ to F_{em}, which represents the number of photons transporting to the LSC edge region relative to the number of photons initially generated and trapped upon the illumination of the LSC surface region:

$$F_{em} = \frac{\int F_{edge}(\lambda)d\lambda}{A_{in} \times \int [1 - T(\lambda)]\varphi_{in}(\lambda)d\lambda \times \Phi_f \times \cos\theta_c} \quad (4)$$

where A_{in} is the area of the hole in the mask (i.e., 6.4516 cm^2) as shown in Fig. 6a; $T(\lambda)$ is the transmission spectrum of the LSC as shown in Fig. 6f; $\varphi(\lambda)$ is the incident photon spectrum (Xenon lamp with AM1.5G filter) as shown in Fig. 6g; $<\Phi_f>$ is the average photoluminescence quantum yield of R305 (i.e., 0.85) as shown in Fig. 6h [20,67]; and θ_c is the critical angle for photon surface escape (i.e., 42.2°) as shown in Fig. 6i [54–59].

The relationship between F_{em} and the surface distance (d_{surf}) in Fig. 6j shows that F_{em} first exhibits a rapid decrease followed by a very slow decay with the increase of d_{surf}. It can be concluded from Fig. 6d and j that a surface distance of 5 inches is possibly the limit for photon transport loss inside the LSC. Within 5 inches, there is severe photon transport loss due to the luminophore self-absorption. Therefore, the emission wavelength of the edge region (λ_{em}) significantly increases, while the corresponding fraction of photons transporting to the edge region (F_{em}) significantly decreases. Beyond 5 inches, both parameters reach a plateau, suggestive of no more luminophore self-absorption. According to the literature [54–59], the relationship between F_{em} and d_{surf} can be represented using an analytical model as shown Eq. (5):

$$F_{em} = \frac{1}{N_{abs}^{<L_{ptn}>_{max}} \times d_{surf} - \sec^2\theta_c} \quad (5)$$

where $N_{abs}^{<L_{ptn}>_{max}}$ is the number of absorption (initial absorption + self-absorption) events that occur at the maximum average photon transport distance.

The parameter $N_{abs}^{<L_{ptn}>_{max}}$ is explained in detail here. Fig. 6k shows the photon transport path of a randomly simulated photon, which transports from the LSC surface to the LSC edge, as an example. As indicated as blue dots, this photon experiences absorption event for 3 times (i.e., $N_{abs} = 3$) and transport 1.143 inches (i.e., $L_{ptn} = 1.143$ inches) inside the LSC. For photons that exhibit the same number of absorption events, $<L_{ptn}>$ represents the average photon transport distance. Through the simulation, the correlation between $<L_{ptn}>$ and N_{abs} at varying LSC size is established as shown in Fig. 6l. It is surprising to see that the maximum $<L_{ptn}>$ ($<L_{ptn}>_{max}$) is independent of N_{abs} as well as the LSC size, and the N_{abs} at $<L_{ptn}>_{max}$ ($N_{abs}^{<L_{ptn}>_{max}}$) is between 11 and 13 (green area in Fig. 6l). This indicates that photons with the average longest

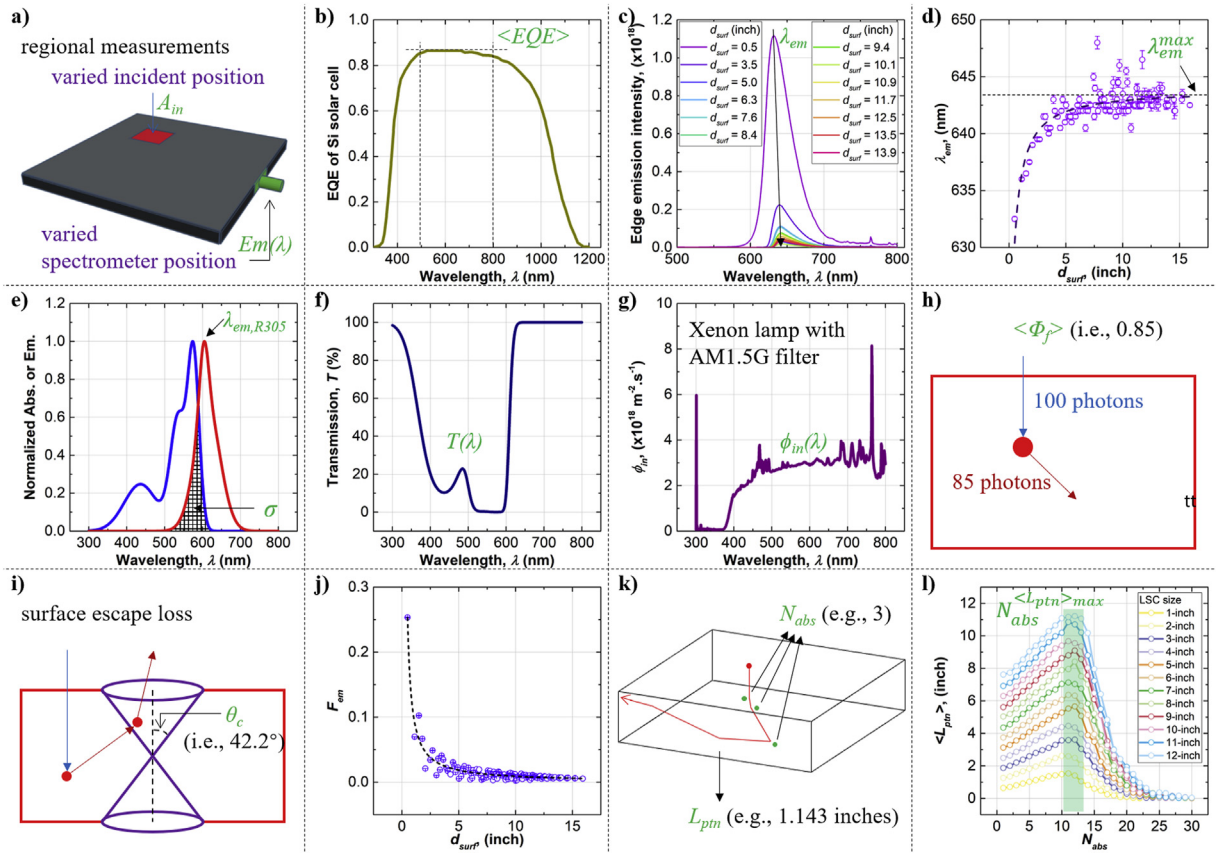

Fig. 6. **a)** Experimental setup of the regional measurements using a photoluminescence (PL) spectrometer. **b)** The definition of <*EQE*>. **c)** $F_{edge}(\lambda)$ at 13 representative d_{surf} and the definition of λ_{em}. **d)** Relationship between λ_{em} and d, fitted curve (dashed line) and the definition of λ_{em}^{max}. **e)** Absorption and emission spectra of R305, and the definitions of $\lambda_{em,R305}$ and σ. **f)** The transmission spectrum of the LSC. **g)** The incident photon spectrum. **h)** The definition of $<\Phi_f>$. **i)** The definition of θ_c. **j)** Relationship between F_{em} and d, and fitted curve (dashed line). **k)** Example of photon transport path showing the definitions of N_{abs} and L_{ptn}. **l)** Relationship between $<L_{ptn}>$ and N_{abs} at varying LSC size.

Table 3
The values of fitting parameters in Eq. (3) and Eq. (5) from the experiment using the regional measurements compared with those from the calculation and simulation.

	λ_{em} vs. d		F_{em} vs. d	
	λ_{em}^{max}, nm	σ	$N_{abs}^{<L_{ptn}>_{max}}$	θ_c (°)
Exp.	643.9 ± 0.3	26.6% ± 4.5%	11.3 ± 0.1	39.3 ± 6.9
Cal./Sim.	645	26%	11–13[a]	42.2

transport distance experience absorption events between 11 and 13 times.

The dashed line in Fig. 6j represents the fitting results. According to Table 3, the fitting parameter $N_{abs}^{<L_{ptn}>_{max}}$ is 11.3 ± 0.1, which is consistent with that from the simulation ($N_{abs}^{<L_{ptn}>_{max}}$ = 11–13 in Fig. 6l). The other fitting parameter θ_c is 39.3° ± 6.9°, which well matches the calculated value (θ_c = 42.2° [54–59]). The results indicate that the regional measurements can reveal key parameters about the photon transport inside the LSCs, which are difficult to access through the conventional method.

5. Conclusions

In summary, we introduced a new methodology to realize the analysis of large-area luminescent solar concentrators (LSCs) (up to 929.0304 cm^2) using basic laboratory instruments including a low-cost solar simulator, a small-area solar cell, and a general photoluminescence (PL) spectrometer. In this methodology, the LSC surface was configured with a mask to have different surface regions, and the LSC edge was configured with a blackout tape and a solar cell/PL spectrometer to have different edge regions. Illumination was sequentially applied to the surface regions, and measurements were sequentially performed at the edge regions. PV performance, especially power conversion efficiencies (PCEs) of a series of R305-based LSCs were studied through the regional measurements. The results were compared with those from the conventional method on small-area LSCs (<200 cm^2) and those from Monte Carlo ray-tracing simulation on large-area LSCs (>200 cm^2). Besides, the results from the regional measurements deeply revealed the photon transport mechanism of the LSCs. The experimental results were fitted with analytical models, which suggested that a surface distance (d_{surf}) of 5 inches (12.7 cm) was possibly the limit of the photon transport loss. Beyond 5 inches, the major photon transport loss due to the luminophore self-absorption became minimal. The results also established a correlation between the average transport distance ($<L_{ptn}>$) and the number of absorption events (N_{abs}) of the photons. Photons with the longest $<L_{ptn}>$ ($<L_{ptn}>_{max}$) were typically associated with N_{abs} of 11.3 despite the LSC size. This report demonstrated that the approach of regional measurements is effective in the study of the PV performance and the photon transport mechanism of large-area LSCs. This approach can be easily applied to any LSCs with rectangle shapes, which are the most widely studied geometries in current research. Future work includes modifying the experimental setup so that LSCs with other shapes (e.g., polygon, cylinder) can be analyzed.

CRediT authorship contribution statement

Yilin Li: Conceptualization, Writing - review & editing, Supervision. **Yujian Sun:** Investigation, Writing - original draft, Visualization. **Yongcao Zhang:** Software, Formal analysis, Data curation.

Declaration of competing interest

The authors declare that they have no known competing financial interests or personal relationships that could have appeared to influence the work reported in this paper.

Acknowledgments

This work is a part of the project: Energy-harvesting windows and panels. The authors would like to thank Solera City Energy for research support.

References

[1] M.G. Debije, P.P.C. Verbunt, Thirty years of luminescent solar concentrator research: solar energy for the built environment, Adv. Energy Mater. 2 (1) (2012) 12–35, https://doi.org/10.1002/aenm.201100554.
[2] F. Meinardi, F. Bruni, S. Brovelli, Luminescent solar concentrators for building-integrated photovoltaics, Nat. Rev. Mater. 2 (2017) 17072, https://doi.org/10.1038/natrevmats.2017.72.
[3] P. Moraitis, R.E.I. Schropp, W.G.J.H.M. van Sark, Nanoparticles for luminescent solar concentrators - a review, Opt. Mater. 84 (2018) 636–645, https://doi.org/10.1016/j.optmat.2018.07.034.
[4] Y. Li, X. Zhang, Y. Zhang, R. Dong, C.K. Luscombe, Review on the role of polymers in luminescent solar concentrators, J. Polym. Sci. 57 (3) (2019) 201–215, https://doi.org/10.1002/pola.29192.
[5] M. Rafiee, S. Chandra, H. Ahmed, S.J. McCormack, An overview of various configurations of Luminescent Solar Concentrators for photovoltaic applications, Opt. Mater. 91 (2019) 212–227, https://doi.org/10.1016/j.optmat.2019.01.007.
[6] Y. Zhao, R.R. Lunt, Transparent luminescent solar concentrators for large-area solar windows enabled by massive Stokes-shift nanocluster phosphors, Adv. Energy Mater. 3 (9) (2013) 1143–1148, https://doi.org/10.1002/aenm.201300173.
[7] Y. Zhao, G.A. Meek, B.G. Levine, R.R. Lunt, Near-Infrared harvesting transparent luminescent solar concentrators, Adv. Opt. Mater. 2 (7) (2014) 606–611, https://doi.org/10.1002/adom.201400103.
[8] C. Yang, J. Zhang, W.T. Peng, W. Sheng, D. Liu, P.S. Kuttipillai, M. Young, M.R. Donahue, B.G. Levine, B. Borhan, R.R. Lunt, Impact of Stokes shift on the performance of near-infrared harvesting transparent luminescent solar concentrators, Sci. Rep. 8 (1) (2018) 16359, https://doi.org/10.1038/s41598-018-34442-3.
[9] A. Kerrouche, D.A. Hardy, D. Ross, B.S. Richards, Luminescent solar concentrators: from experimental validation of 3D ray-tracing simulations to coloured stained-glass windows for BIPV, Sol. Energy Mater. Sol. Cells 122 (2014) 99–106, https://doi.org/10.1016/j.solmat.2013.11.026.
[10] C. Corrado, S.W. Leow, M. Osborn, I. Carbone, K. Hellier, M. Short, G. Alers, S.A. Carter, Power generation study of luminescent solar concentrator greenhouse, J. Renew. Sustain. Energy 8 (4) (2016), https://doi.org/10.1063/1.4958735, 043502.
[11] W. van Sark, P. Moraitis, C. Aalberts, M. Drent, T. Grasso, Y. L'Ortije, M. Visschers, M. Westra, R. Plas, W. Planje, The "electric mondrian" as a luminescent solar concentrator demonstrator case study, Solar RRL 1 (3-4) (2017) 1600015, https://doi.org/10.1002/solr.201600015.
[12] L. Zalewski, S. Lassue, B. Duthoit, M. Butez, Study of solar walls - validating a simulation model, Build. Environ. 37 (1) (2002) 109–121, https://doi.org/10.1016/S0360-1323(00)00072-X.
[13] J.V. Akwa, O. Konrad, G.V. Kaufmann, C.A. Machado, Evaluation of the photovoltaic generation potential and real-time analysis of the photovoltaic panel operation on a building facade in southern Brazil, Energy Build. 69 (2014) 426–433, https://doi.org/10.1016/j.enbuild.2013.11.007.
[14] C.-M. Lai, S. Hokoi, Solar façades: a review, Build. Environ. 91 (2015) 152–165, https://doi.org/10.1016/j.buildenv.2015.01.007.
[15] Y. Li, C. Liu, Techno-economic analysis for constructing solar photovoltaic projects on building envelopes, Build. Environ. 127 (2018) 37–46, https://doi.org/10.1016/j.buildenv.2017.10.014.
[16] D. Powell, I. Hischier, P. Jayathissa, B. Svetozarevic, A. Schlüter, A reflective adaptive solar façade for multi-building energy and comfort management, Energy Build. 177 (2018) 303–315, https://doi.org/10.1016/j.enbuild.2018.07.040.
[17] H. Kang, T. Hong, S. Jung, M. Lee, Techno-economic performance analysis of the smart solar photovoltaic blinds considering the photovoltaic panel type and the solar tracking method, Energy Build. 193 (2019) 1–14, https://doi.org/10.1016/j.enbuild.2019.03.042.
[18] M.G. Debije, V.A. Rajkumar, Direct versus indirect illumination of a prototype luminescent solar concentrator, Sol. Energy 122 (2015) 334–340, https://doi.org/10.1016/j.solener.2015.08.036.
[19] F.M. Vossen, M.P.J. Aarts, M.G. Debije, Visual performance of red luminescent solar concentrating windows in an office environment, Energy Build. 113 (2016) 123–132, https://doi.org/10.1016/j.enbuild.2015.12.022.
[20] Y. Li, Y. Sun, Y. Zhang, Luminescent solar concentrators performing under different light conditions, Sol. Energy 188 (2019) 1248–1255, https://doi.org/10.1016/j.solener.2019.07.035.
[21] A. Sanguineti, M. Sassi, R. Turrisi, R. Ruffo, G. Vaccaro, F. Meinardi, L. Beverina, High Stokes shift perylene dyes for luminescent solar concentrators, Chem. Commun. 49 (16) (2013) 1618–1620, https://doi.org/10.1039/c2cc38708e.
[22] Y.E. Mouedden, B. Ding, Q. Song, G. Li, H. Nguyen, K. Alameh, A cost-effective, long-lifetime efficient organic luminescent solar concentrator, J. Appl. Phys. 118 (2015), https://doi.org/10.1063/1.4923389, 015502.
[23] Y. Li, J. Olsen, K. Nunez-Ortega, W.-J. Dong, A structurally modified perylene dye for efficient luminescent solar concentrators, Sol. Energy 136 (2016) 668–674, https://doi.org/10.1016/j.solener.2016.07.051.
[24] F. Purcell-Milton, Y.K. Gun'ko, Quantum dots for luminescent solar concentrators, J. Mater. Chem. 22 (33) (2012) 16687–16697, https://doi.org/10.1039/c2jm32366d.
[25] Y. Zhou, H. Zhao, D. Ma, F. Rosei, Harnessing the properties of colloidal quantum dots in luminescent solar concentrators, Chem. Soc. Rev. 47 (15) (2018) 5866–5890, https://doi.org/10.1039/c7cs00701a.
[26] Z. Li, X. Zhao, C. Huang, X. Gong, Recent advances in green fabrication of luminescent solar concentrators using nontoxic quantum dots as fluorophores, J. Mater. Chem. C 7 (40) (2019) 12373–12387, https://doi.org/10.1039/C9TC03520F.
[27] C. Liu, R. Deng, Y. Gong, C. Zou, Y. Liu, X. Zhou, B. Li, Luminescent solar concentrators fabricated by dispersing rare earth particles in PMMA waveguide, Int. J. Photoenergy 2014 (2014) 290952, https://doi.org/10.1155/2014/290952.
[28] V.T. Freitas, L. Fu, A.M. Cojocariu, X. Cattoën, J.R. Bartlett, R.L. Parc, J.-L. Bantignies, M.W.C. Man, P.S. André, R.A.S. Ferreira, L.D. Carlos, Eu^{3+}-based bridged silsesquioxanes for transparent luminescent solar concentrators, ACS Appl. Mater. Interfaces 7 (16) (2015) 8770–8778, https://doi.org/10.1021/acsami.5b01281.
[29] A.R. Frias, M.A. Cardoso, A.R.N. Bastos, S.F.H. Correia, P.S. André, L.D. Carlos, V.d.Z. Bermudez, R.A.S. Ferreira, Transparent luminescent solar concentrators using Ln^{3+}-based ionosilicas towards photovoltaic windows, Energies 12 (3) (2019) 451, https://doi.org/10.3390/en12030451.
[30] T.A. Cohen, T.J. Milstein, D.M. Kroupa, J.D. MacKenzie, C.K. Luscombe, D.R. Gamelin, Quantum-cutting Yb^{3+}-doped perovskite nanocrystals for monolithic bilayer luminescent solar concentrators, J. Mater. Chem. 7 (5) (2019) 9279–9288, https://doi.org/10.1039/C9TA01261C.
[31] H. Zhao, R. Sun, Z. Wang, K. Fu, X. Hu, Y. Zhang, Zero-dimensional perovskite nanocrystals for efficient luminescent solar concentrators, Adv. Funct. Mater. 29 (30) (2019) 1902262, https://doi.org/10.1002/adfm.201902262.
[32] Z. Li, A. Johnston, M. Wei, M.I. Saidaminov, J.M.d. Pina, X. Zheng, J. Liu, Y. Liu, O.M. Bakr, E.H. Sargent, Solvent-solute coordination engineering for efficient perovskite luminescent solar concentrators, Joule 4 (3) (2020) 631–643, https://doi.org/10.1016/j.joule.2020.01.003.
[33] J.K. Tseng, Y.J. Chen, C.T. Pan, T.T. Wu, M.H. Chung, Application of optical film with micro-lens array on a solar concentrator, Sol. Energy 85 (9) (2011) 2167–2178, https://doi.org/10.1016/j.solener.2011.06.004.
[34] P. Damrongsak, K. Locharoenrat, Optical performance of fluorescent collectors integrated with microlens arrays, Mater. Res. Express 4 (9) (2017), https://doi.org/10.1088/2053-1591/aa8a1b, 095502.
[35] I. Kurmi, D.C. Schedl, O. Bimber, Micro-lens aperture array for enhanced thin-film imaging using luminescent concentrators, Optic Express 26 (2) (2018) 29253–29261, https://doi.org/10.1364/oe.26.029253.
[36] S. Chandra, J. Doran, S.J. McCormack, M. Kennedy, A.J. Chattenc, Enhanced quantum dot emission for luminescent solar concentrators using plasmonic interaction, Sol. Energy Mater. Sol. Cells 98 (2012) 385–390, https://doi.org/10.1016/j.solmat.2011.11.030.
[37] C. Tummeltshammer, M.S. Brown, A. Taylor, A.J. Kenyon, I. Papakonstantinou, Efficiency and loss mechanisms of plasmonic luminescent solar concentrators, Optic Express 21 (S5) (2013) A735–A749, https://doi.org/10.1364/oe.21.00a735.
[38] M. Fahad, H. Oh, W. Jung, M. Binns, S.-K. Hong, Metal nanoparticles based stack structured plasmonic luminescent solar concentrator, Sol. Energy 155 (2017) 934–941, https://doi.org/10.1016/j.solener.2017.07.037.
[39] M.G. Debije, M.P. Van, P.P. Verbunt, M.J. Kastelijn, R.H. van der Blom, D.J. Broer, C.W. Bastiaansen, Effect on the output of a luminescent solar concentrator on application of organic wavelength-selective mirrors, Appl. Optic. 49 (4) (2010) 745–751, https://doi.org/10.1364/ao.49.000745.
[40] P.P. Verbunt, S. Tsoi, M.G. Debije, D.J. Broer, C.W. Bastiaansen, C.W. Lin, D.K. de Boer, Increased efficiency of luminescent solar concentrators after application of organic wavelength selective mirrors, Optic Express 20 (S5) (2012) A655–A668, https://doi.org/10.1364/oe.20.00a655.
[41] R. Connell, C. Pinnell, V.E. Ferry, Designing spectrally-selective mirrors for use in luminescent solar concentrators, J. Optic. 20 (2) (2018), 024009, https://doi.org/10.1088/2040-8986/aaa074.
[42] L. Xu, Y. Yao, N.D. Bronstein, L. Li, A.P. Alivisatos, R.G. Nuzzo, Enhanced photon

collection in luminescent solar concentrators with distributed bragg reflectors, ACS Photonics 3 (2) (2016) 278–285, https://doi.org/10.1021/acsphotonics.5b00630.
[43] R. Connell, V.E. Ferry, Integrating photonics with luminescent solar concentrators: optical transport in the presence of photonic mirrors, J. Phys. Chem. C 120 (37) (2016) 20991–20997, https://doi.org/10.1021/acs.jpcc.6b03304.
[44] G. Iasilli, R. Francischello, P. Lova, S. Silvano, A. Surace, G. Pesce, M. Alloisio, M. Patrini, M. Shimizu, D. Comoretto, A. Pucci, Luminescent solar concentrators: boosted optical efficiency by polymer dielectric mirrors, Mater. Chem. Front. 3 (3) (2019) 429–436, https://doi.org/10.1039/c8qm00595h.
[45] L.H. Slooff, E.E. Bende, A.R. Burgers, T. Budel, M. Pravettoni, R.P. Kenny, E.D. Dunlop, A. Büchtemann, A luminescent solar concentrator with 7.1% power conversion efficiency, Phys. Status Solidi RRL 2 (6) (2008) 257–259, https://doi.org/10.1002/pssr.200802186.
[46] J.C. Goldschmidt, M. Peters, A. Bösch, H. Helmers, F. Dimroth, S.W. Glunz, G. Willeke, Increasing the efficiency of fluorescent concentrator systems, Sol. Energy Mater. Sol. Cells 93 (2) (2009) 176–182, https://doi.org/10.1016/j.solmat.2008.09.048.
[47] L. Desmet, A.J. Ras, D.K. de Boer, M.G. Debije, Monocrystalline silicon photovoltaic luminescent solar concentrator with 4.2% power conversion efficiency, Opt. Lett. 37 (15) (2012) 3087–3089, https://doi.org/10.1364/ol.37.003087.
[48] C. Tummeltshammer, A. Taylor, A.J. Kenyon, I. Papakonstantinou, Losses in luminescent solar concentrators unveiled, Sol. Energy Mater. Sol. Cells 144 (2016) 40–47, https://doi.org/10.1016/j.solmat.2015.08.008.
[49] V.I. Klimov, T.A. Baker, J. Lim, K.A. Velizhanin, H. McDaniel, Quality factor of luminescent solar concentrators and practical concentration limits attainable with semiconductor quantum dots, ACS Photonics 3 (6) (2016) 1138–1148, https://doi.org/10.1021/acsphotonics.6b00307.
[50] A.R. Frias, E. Pecoraro, S.F.H. Correia, L.M.G. Minas, A.R. Bastos, S. García-Revilla, R. Balda, S.J.L. Ribeiro, P.S. André, L.D. Carlos, R.A.S. Ferreira, Sustainable luminescent solar concentrators based on organic-inorganic hybrids modified with chlorophyll, J. Mater. Chem. 6 (18) (2018) 8712–8723, https://doi.org/10.1039/C8TA01712C.
[51] M. Kanellis, M.M.d. Jong, L. Slooff, M.G. Debije, The solar noise barrier project: 1. Effect of incident light orientation on the performance of a large-scale luminescent solar concentrator noise barrier, Renew. Energy 103 (2017) 647–652, https://doi.org/10.1016/j.renene.2016.10.078.
[52] M.G. Debije, C. Tzikas, V.A. Rajkumar, M.M.d. Jong, The solar noise barrier project: 2. The effect of street art on performance of a large scale luminescent solar concentrator prototype, Renew. Energy 113 (2017) 1288–1292, https://doi.org/10.1016/j.renene.2017.07.025.
[53] M.G. Debije, C. Tzikas, M.M.d. Jong, M. Kanellis, L.H. Slooff, The solar noise barrier project: 3. The effects of seasonal spectral variation, cloud cover and heat distribution on the performance of full-scale luminescent solar concentrator panels, Renew. Energy 116A (2017) 335–343, https://doi.org/10.1016/j.renene.2017.09.079.
[54] J.S. Batchelder, A.H. Zewail, T. Cole, Luminescent solar concentrators. 1: theory of operation and techniques for performance evaluation, Appl. Optic. 18 (18) (1979) 3090–3110, https://doi.org/10.1364/AO.18.003090.
[55] J.S. Batchelder, A.H. Zewail, T. Cole, Luminescent solar concentrators. 2: experimental and theoretical analysis of their possible efficiencies, Appl. Optic. 20 (21) (1981) 3733–3754, https://doi.org/10.1364/AO.20.003733.
[56] K. Barnham, J.L. Marques, J. Hassard, Quantum-dot concentrator and thermodynamic model for the global redshift, Appl. Phys. Lett. 76 (9) (2000) 1197, https://doi.org/10.1063/1.125981.
[57] T. Wang, B. Yu, B. Chen, Z. Hu, Y. Luo, G. Zou, Q. Zhang, A theoretical model of a cylindrical luminescent solar concentrator with a dye-doping coating, J. Optic. 15 (5) (2013), https://doi.org/10.1088/2040-8978/15/5/055709, 055709.
[58] A.-L. Joudrier, F. Proise, R. Grapin, J.-L. Pelouard, J.-F. Guillemoles, Modeling and fabrication of luminescent solar concentrators towards photovoltaic devices, Energy Procedia 60 (2014) 173–180, https://doi.org/10.1016/j.egypro.2014.12.360.
[59] I. Sychugov, Analytical description of a luminescent solar concentrator, Optica 6 (8) (2019) 1046–1049, https://doi.org/10.1364/OPTICA.6.001046.
[60] L.R. Wilson, B.C. Rowan, N. Robertson, O. Moudam, A.C. Jones, B.S. Richards, Characterization and reduction of reabsorption losses in luminescent solar concentrators, Appl. Optic. 49 (9) (2010) 1651–1661, https://doi.org/10.1364/ao.49.001651.
[61] G. Griffini, M. Levi, StefanoTurri, Novel crosslinked host matrices based on fluorinated polymers for long-term durability in thin-film luminescent solar concentrators, Sol. Energy Mater. Sol. Cells 118 (2013) 36–42, https://doi.org/10.1016/j.solmat.2013.05.041.
[62] P.D. Sala, N. Buccheri, A. Sanzone, M. Sassi, P. Neri, C. Talotta, A. Rocco, V. Pinchetti, L. Beverina, S. Brovelli, C. Gaeta, First demonstration of the use of very large Stokes shift cycloparaphenylenes as promising organic luminophores for transparent luminescent solar concentrators, Chem. Commun. 55 (21) (2019) 3160–3163, https://doi.org/10.1039/c8cc09859j.
[63] D. Sahin, B. Ilan, D.F. Kelley, Monte-Carlo simulations of light propagation in luminescent solar concentrators based on semiconductor nanoparticles, J. Appl. Phys. 110 (3) (2011), https://doi.org/10.1063/1.3619809.
[64] S.W. Leow, C. Corrado, M. Osborn, M. Isaacson, G. Alers, S.A. Carter, Analyzing luminescent solar concentrators with front-facing photovoltaic cells using weighted Monte Carlo ray tracing, J. Appl. Phys. 113 (21) (2013), https://doi.org/10.1063/1.4807413.
[65] J.P. Shu, X.W. Zhang, P.J. Wang, R.W. Chen, H.H. Zhang, D.K. Li, P. Zhang, J. Xu, Monte-Carlo simulations of optical efficiency in luminescent solar concentrators based on all-inorganic perovskite quantum dots, Physica B 548 (2018) 53–57, https://doi.org/10.1016/j.physb.2018.08.021.
[66] Z. Krumer, S.J. Pera, R.J.A.v. Dijk-Moes, Y. Zhao, A.F.P.d. Brouwer, E. Groeneveld, W.G.J.H.M. van Sark, R.E.I. Schropp, C.M. Donegá, Tackling self-absorption in luminescent solar concentrators with type-II colloidal quantum dots, Sol. Energy Mater. Sol. Cells 111 (2013) 57–65, https://doi.org/10.1016/j.solmat.2012.12.028.
[67] Y. Li, Y. Sun, Y. Zhang, Boosting the cost-effectiveness of luminescent solar concentrators through subwavelength sanding treatment, Sol. Energy 198 (2020) 151–159, https://doi.org/10.1016/j.solener.2020.01.038.